Mapping and characterizing thermal dilation of civil infrastructures with multi-temporal X-band synthetic Aperture Radar interferometry

Qin, Xiaoqiong; Zhang, Lu; Ding, Xiaoli; Liao, Mingsheng; Yang, Mengshi

Important note
To cite this publication, please use the final published version (if applicable).
Please check the document version above.

Mapping and Characterizing Thermal Dilation of Civil Infrastructures with Multi-Temporal X-Band Synthetic Aperture Radar Interferometry

Xiaoqiong Qin [1,2], **Lu Zhang** [1] iD, **Xiaoli Ding** [2], **Mingsheng Liao** [1,3,*] **and Mengshi Yang** [1,4] iD

[1] State Key Laboratory of Information Engineering in Surveying, Mapping and Remote Sensing, Wuhan University, Wuhan 430079, China; qinxiaoqiong@whu.edu.cn (X.Q.); luzhang@whu.edu.cn (L.Z.); yangms@whu.edu.cn (M.Y.)

[2] Department of Land Surveying and Geo-Informatics, The Hong Kong Polytechnic University, Hung Hom, KLN, Hong Kong, China; xl.ding@polyu.edu.hk

[3] Key Laboratory of Land Subsidence Monitoring and Prevention, Ministry of Land and Resources of China, Shanghai 200072, China

[4] Department of Geoscience and Remote Sensing, Delft University of Technology, 2628CN Delft, The Netherlands

[*] Correspondence: liao@whu.edu.cn; Tel.: +86-27-68778070

check for updates

Abstract: Temperature variation plays a significant role in the long-term structural behaviour of civil infrastructures, but very few quantitative studies have measured and analysed the infrastructures' global thermal dilation because of their large sizes and geometric complexities. The modern Differential Synthetic Aperture Radar Interferometry (DInSAR) technique has great potential in applications of their thermal dilation mapping and characterization due to the techniques' unique capabilities for use in large areas, with high-resolution, and at low-costs for deformation measurements. However, the practical application of DInSAR in thermal dilation estimation is limited by difficulty in the precise separation from the residual topographic phase and the trend deformation phase. Moreover, due to a lack of thermal dilation characteristics analyses in previous studies, the thermal dilation mechanisms are still unclear to users, which restricts the accurate understanding of the thermal dilation evolution process. Given the above challenges, an advanced multi-temporal DInSAR approach is proposed in this study, and the effectiveness of this approach was presented using three cases studies concerning different infrastructure types. In this method, the coherent, incoherent, and semantic information of structures were combined in order to refine the detection of point-like targets (PTs). Interferometric subsets with small temporal baselines and temperature differences were used for high-resolution topography estimation. A pre-analysis was adopted to determine the transmission direction, spatial pattern, and temporal variation of the thermal dilation. Then, both the traditional least squares estimation and our robust coherence-weighted least squares regression analysis were performed between the time series displacements and the corresponding temperatures to quantitatively estimate the thermal dilation model. The results were verified in terms of the estimated linear thermal dilation coefficient, which indicates the greater reliability of our method. Furthermore, the thermal dilation characteristics of different civil infrastructure types were analysed, which facilitates a greater understanding of the thermal dilation evolution process of civil infrastructures.

Keywords: thermal dilation characteristics; civil infrastructures; multi-temporal DInSAR analysis; TerraSAR-X; least squares

1. Introduction

The widespread deterioration and the inadequate upkeep of existing civil infrastructures, such as buildings, highways, and bridges, has accelerated the growing costs of their replacements and repairs, and also brought significant risks to public safety and quality of life [1,2]. To ensure the safe operations of these infrastructures and to reduce the maintenance costs, the consecutive stability monitoring of such manmade structures in an economical manner is important, especially in densely inhabited areas, to detect the deformation at an early stage and to prevent the associated risks by taking timely measures [3,4]. However, it is difficult to achieve this goal using current in situ methods for civil infrastructure monitoring because most in situ techniques (e.g., leveling and total station surveys) are labour-intensive and not frequently performed [5,6]. Currently, professionals and technical officers are seeking sustainable solutions for the routine inspections of civil infrastructures with reduced human resources and allocated funds.

Fortunately, the satellite-based multi-temporal Differential Interferometry Synthetic Aperture Radar (DInSAR) technique offers the unique potential for large area and millimetre-level surface deformation monitoring under all day and during all weather conditions [7–10]. Moreover, several improvements in both the techniques and data quality led to more effective long-term deformation monitoring [6–8,11–17]. In particular, the X-band satellite missions that were launched in June 2007 provide high-resolution X-band SAR data for scientific and commercial purposes. The short wavelength of 3.1 cm, short revisit cycles, and high resolution of 3 m in Stripmap mode considerably distinguishes this data from previous civil SAR systems, enabling the detailed monitoring of civil infrastructures [18–25].

According to previous studies, the temperature variation is considered to have a more significant effect on the deformation of civil infrastructures than the effects of operation loads or structural damage [19,26,27]. Given the high sensitivity of the X-band SAR data on thermal expansion, the expanding or contracting of materials owing to temperature variation would cause a strong seasonal variation in the DInSAR time series displacements, especially when metallic components comprise most of the structure [19,28–34]. Moreover, during the multi-temporal DInSAR monitoring, when the observation period does not correspond to exactly one year or an integral multiple of one year, this periodical displacement would also lead to a non-zero deformation signal of point-like targets (PTs) [30–32]. As a result, the thermal dilation of civil infrastructures must be incorporated into DInSAR processing and interpretation in order to reliably detect infrastructural trend deformation.

Although many studies have dealt with thermal dilation estimation during time series DInSAR monitoring [19,28–34], a number of technical challenges also appeared. First, only a few studies have considered the resolution gap between the X-band SAR images (approximately 3 m) and the old Shuttle Radar Topography Mission (SRTM) (approximately 30 m) [20,35], which would cause uncertainties in the estimated topography, especially for infrastructures newly built after 2000, which affects the accuracy of the thermal dilation and trend deformation mapping. In addition, most of the previous studies ceased at the separation of the thermal dilation, rather than going deep into the investigation of thermal dilation characteristics, such as the transmission direction, spatial pattern, and magnitude, which means that the thermal dilation mechanisms remain unclear to users. Thus, challenges in better understanding the thermal dilation evolution process of civil infrastructures continue.

To address the existing issues that are illustrated above, a multi-temporal DInSAR analysis approach that is aimed at mapping and characterizing the thermal dilation of different infrastructure types, using denser PTs and more accurate topographic phase estimation, is proposed and applied in this study. In this method, the coherent, incoherent, and semantic information of structures were comprehensively considered to improve the density and accuracy of detectable PTs upon structures. Moreover, a high-resolution topography was estimated from the interferometric subsets with small temporal baselines and temperature differences, which eliminates the possible uncertainties of topography estimation and the effects of uncertainties on deformation mapping. Then, a two-step analysis method, which consists of a model analysis phase and a model generation phase,

was implemented to estimate the thermal dilation. First, the time series differential interferometric phases were visually pre-analysed in order to qualitatively investigate the possible transmission direction, spatial pattern, and temporal variation of the thermal dilation. Then, the pre-analysed results were used in the model generation phase. With the assumption that temperature is homogeneous along the structure, both the traditional least squares regression analysis and the robust coherence-weighted least squares regression analysis that is proposed in this study were implemented to establish the thermal dilation model. Finally, the thermal dilation models estimated from the two methods were verified by comparing the estimated linear thermal dilation coefficients against the actual physical properties of materials, which indicates the greater reliability of our method.

Based on the above approach, three case studies concerning different infrastructures types, including the skyscraper buildings, low buildings, and linear highways, were carried out and are discussed in this article. The experimental results demonstrated the effectiveness of the proposed method for the thermal dilation mapping of different infrastructure types, and the deformation maps of thermal dilation and trend deformation were separately produced. The thermal dilation characteristics, such as the transmission direction, spatial pattern, and magnitude were captured by comparing the thermal dilation results with the different structural information, including specific structural shapes, mechanical properties, construction materials, and sizes. Our results demonstrated that the transmission direction of the thermal dilation is highly dependent on the specific structural shape of the target, which is usually along the direction of the longest side of the geometric shape. Moreover, the static structural characteristics of infrastructures, such as the positions of structural key points, can be approximately inferred from the spatial pattern of thermal dilation. Finally, the magnitude of thermal dilation is proven to be highly variable for each infrastructure, which is associated with the material properties and sizes of the objects. These analytical findings provide conclusive evidence of the complex thermal dilation of different infrastructure types and aids in understanding the infrastructures' thermal dilation evolution process.

This paper is structured as follows: Section 2 describes the multi-temporal DInSAR analysis method that is applied in this study. The basic information of study objects, their datasets, and preliminary results are introduced in Section 3. Then, a discussion of the thermal dilation characteristics on different civil infrastructure types is carried out in Section 4. The conclusions are given in Section 5.

2. Methodology

The main workflow of the multi-temporal DInSAR approach that is applied in this paper is illustrated in Figure 1, in which some steps have been improved to refine the thermal dilation monitoring of civil infrastructure using X-band high-resolution SAR images. The main idea of the improved steps marked by the coloured rectangles, including the refined point-like target detection, topographic phase estimation and displacement retrieval, as well as the thermal dilation mapping and characterization, are described in detail in the following.

2.1. Refined Point-Like Target Detection

In practical applications, it is important to maintain the high level of density and accuracy of the selected PTs when monitoring the detailed deformation of ground targets [16–18]. This is because detecting as many PTs as possible on the structures is conducive to reducing the calculation error, as well as improving the estimation accuracy in DInSAR monitoring [7,8,12]. Moreover, since the backscattering signals of different ground targets in the complex urban scenery are usually mixed together due to oblique scene illumination, it is difficult to separate these PTs using the traditional method. Therefore, new methods that are aimed at improving the density and accuracy of detectable PTs upon the civil infrastructures are required for this research. In this study, the coherent and incoherent information derived from the high-resolution SAR images, as well as the detailed semantic information about specific structures are fully integrated into the multi-temporal DInSAR processing to refine detection of PTs.
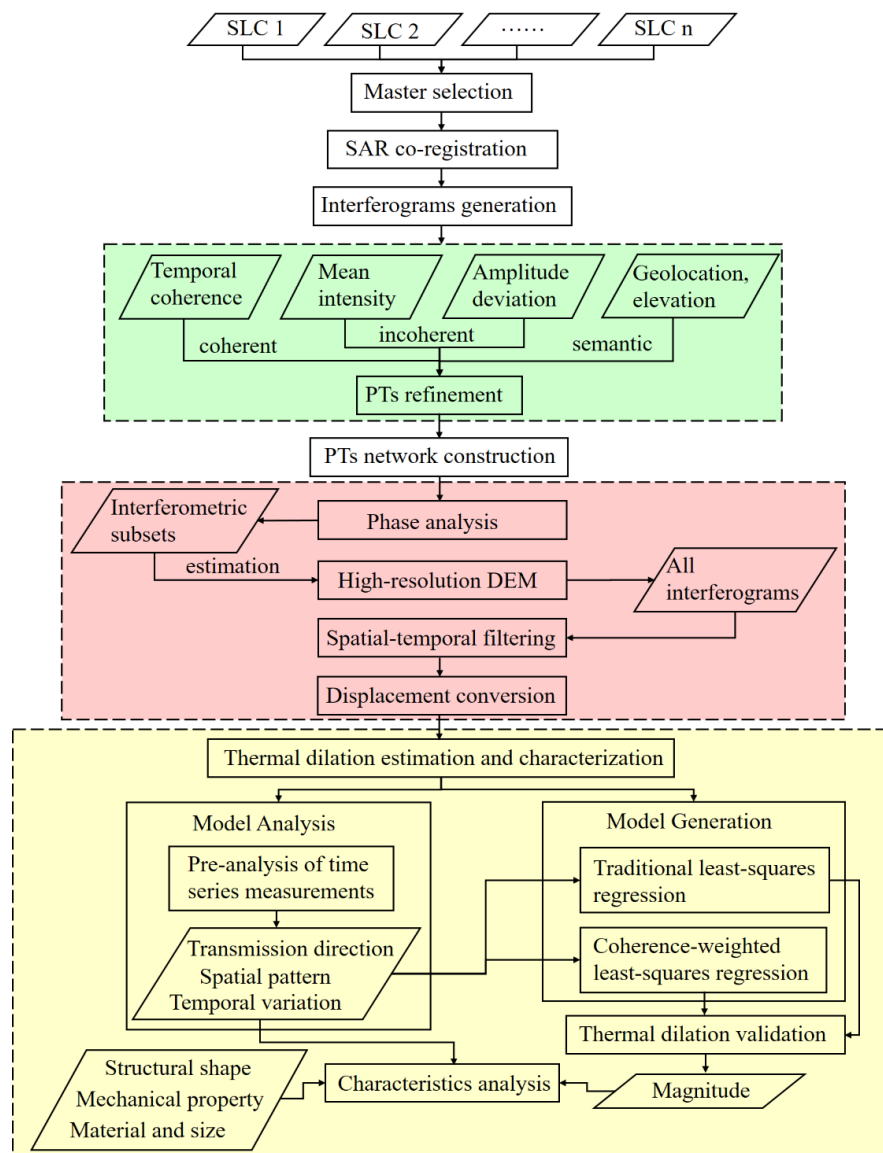
Figure 1. Main workflow of proposed multi-temporal Differential Synthetic Aperture Radar Interferometry (DInSAR) approach.

Since the higher coherence of SAR images usually indicates a higher quality of the interferometric phase, the temporal coherence, which is an indicator of phase stability, was used to select a set of PT candidates [12,13]. On the other hand, the statistical values of backscattering signals, including the mean intensity and the amplitude deviation of the time series SAR images, were also used as independent incoherent information to identify another set of PT candidates. Then, the PT candidates selected from both the coherent and incoherent information are merged to maximize the number of detectable PTs, which is greater than the number of PTs selected by each method alone. The object cognitive abilities of the coherent and incoherent information in the high-resolution SAR images are complemented in this study.

In this study, the specific semantic information of the infrastructures such as geometric shape, geolocation buffer zone, and elevation were integrated together into the PTs refinement [31,36]. First, the PTs located within a local buffer zone of the structures' geolocation in the horizontal plane were chosen as PTs candidates. Then, the outlier points and target points were distinguished according to their local elevation analysis, which improves the accuracy of the structural PTs. Since the PTs

elevation selected on the civil structures should be consecutive, if the difference between the mean elevation of surrounding PTs and the central PT is less than double of their root means squares, the PT is thought to be the target point. Otherwise, the PT would be removed as an outlier point.

2.2. Topographic Phase Estimation and Displacement Retrieval

After PTs refinement, the observed phase of the *i*th PT in the *j*th interferogram can be expressed as Equation (1) [7,9,13]:

$$\varnothing_{int_{i,j}} = \varnothing_{def_{i,j}} + \varnothing_{top_{i,j}} + \varnothing_{atm_{i,j}} + \varnothing_{robit_{i,j}} + \varnothing_{noise_{i,j}} \tag{1}$$

In the above equation, $\varnothing_{int}$ stands for the interferogram phase of the PT; $\varnothing_{def}$ indicates the phase change caused by displacement in the line-of-sight (LOS) direction, $\varnothing_{top}$ represents the topographic phase caused by the height of target; $\varnothing_{atm}$ accounts for the phase contributed by the difference in atmospheric retardation between image pair; and $\varnothing_{orbit}$ corresponds to the phase due to orbit inaccuracy. The noise term $\varnothing_{noise}$ is small enough for a PT and does not significantly obscure the signal [9,10].

The difference in resolution between the SRTM Digital Elevation Model (DEM) and TerraSAR-X data might lead to the inaccurate estimation of the topographic phase, especially for modern civil infrastructures. Therefore, the SRTM DEM must be used cautiously, especially in rapidly developing cities like Shanghai and Hong Kong, and methods of topographic phase estimation should be further improved when aiming at the accurate thermal dilation monitoring of civil infrastructures [20,35]. In this study, the interferometric subsets with temperature differences of less than 2.5 °C and temporal baselines of less than 100 days were used for the high-resolution topography estimation. Although the temperature difference of 2.5 °C may cause thermal dilation, when the temperature is close to the reference temperature (without thermal dilation), the temperature of the infrastructures does not change much with such a small temperature difference and the corresponding thermal dilation can be ignored. Therefore, the deformation phase is supposed to be small, and the atmosphere and noise phases can be separated during the time series processing. Then, the high-resolution topography of the study area can be obtained and used as a high-resolution DEM in order to generate a set of differential interferograms from the total interferograms.

Then, a three-dimensional (3D) time-space unwrapping algorithm is applied to estimate the final deformation of each PT [9,11,13]. The observed deformation, including the linear and nonlinear displacements, can be decomposed into the vertical and horizontal directions for further analysis. The deformation measurement of DInSAR (D_{Los}) is the projection of the original displacement *D* with the components D_{Ver} and D_{Hor} in the vertical and horizontal directions, respectively, on the LOS direction. Assuming that the local incidence angle of the satellite is *θ*, the LOS displacement can be decomposed by the following equation.

$$D_{Los} = D_{Ver} \cdot cos\theta + D_{Hor} \cdot sin\theta \tag{2}$$

Actually, high-resolution SAR datasets, including both ascending and descending tracks, to model a reliable 3D deformation are not always available. Therefore, based on the assumption that the civil infrastructure deformation is mainly caused by the thermal dilation, and the thermal dilation was always transmitted along one direction (either vertically or horizontally), which was also proven in many previous studies [26,37], a simplified conversion of D_{Los} from the LOS direction into the vertical or horizontal directions displacements can be implemented by the following equations:

$$D_{Ver} = D_{Los}/cos\theta \tag{3}$$

$$D_{Hor} = D_{Los}/sin\theta \tag{4}$$

Furthermore, for horizontal civil infrastructures, such as highways, the displacement along the longitudinal direction (D_{Lon}) can be calculated by the following equation:

$$D_{Lon} = D_{Los}/sin\theta cos\alpha \tag{5}$$

Here, α is the horizontal angle between the structure orientation and the LOS direction, as illustrated in Figure 2.
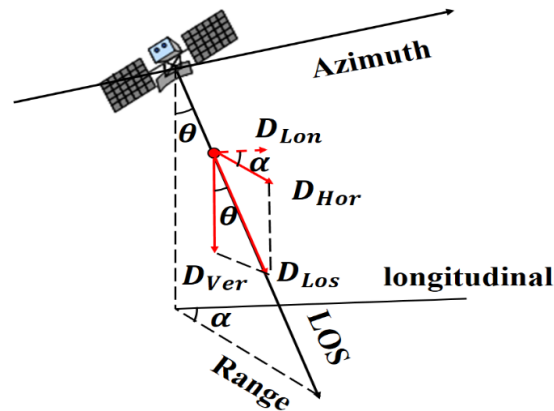

Figure 2. Scheme of displacement detection in Synthetic Aperture Radar (SAR) geometry.

2.3. Thermal Dilation Mapping and Characterization

Since most modern civil infrastructures are constructed by steel or reinforced concrete material, the change in ambient temperature would cause the thermal expansion and contraction of the structure and material, which would even exceed the magnitude of other phase components [20–22,37]. This phenomenon, if not properly handled during the DInSAR data processing and analysis, would have a significant impact on the interferometric products, particularly on the deformation velocity map, and would challenge the widespread application of DInSAR technology for civil infrastructure monitoring [19,28–34,37].

Most previous studies modelled thermal dilation by adding a temperature dependent phase term into the traditional two-dimensional (linear velocity and topographic error) analysis model, or by using a periodic seasonal phase term [19,28,29]. In this study, the deformation signals were estimated through temporal-spatial filtering using the StamPS method [12,13], rather than through calculation with a prior deformation model hypothesis, such as a linear model [7]. Therefore, an additional two-step thermal dilation analysis method was applied to the deformation signals after the estimation of other phase components [31,37].

The two-step thermal dilation analysis method consists of a model analysis phase and a model generation phase. The model analysis phase qualitatively estimates the characteristics of thermal dilation for structures. In our experiments, this step is carried out by visually observing and pre-analysing the characteristics of the time series differential interferometric phases. Critical features that can be detected from the time series differential interferograms are the possible transmission direction, spatial pattern, and temporal variation of thermal dilation.

Then, the above qualitative analysis results were used in the model generation phase. The correlation pattern between the measured time series deformation along the thermal dilation transmission direction and the corresponding temperature variation was quantitatively established with a robust coherence-weighted least squares linear regression fitting [31,37]. In most of the previous

empirical linear models, the regression parameters were commonly computed in order to minimize an error function based on least squares estimates, as in Equation (6):

$$\frac{1}{n} \sum_{i=1}^{n} \left(E_i - \hat{E}_i \right)^2 = \ \text{min} \tag{6}$$

In the above equation, n is the number of observations, E_i indicates the measurement, and $\hat{E}_i$ represents the displacement that is predicted by the estimated model. However, this criterion is known to be sensitive to the presence of outliers in the datasets and therefore may lead to unreliable models [38,39]. In this study, we mitigate this problem by employing a robust weighted least squares function in which weights are assigned to the time series measurements. Since the interferograms with higher coherence would produce more reliable measurements, the use of the interferometric coherence of interferometric pairs to determine the weight of the corresponding time series observations (given by Equation (7)) is simple and effective.

$$\frac{\hat{\gamma}_i}{n} \sum_{i=1}^{n} \left(E_i - \hat{E}_i \right)^2 = \text{min} \tag{7}$$

Here, $\hat{\gamma}_i$ indicates the average coherence of the ith interferogram. The coherence of a pixel in the ith interferogram is calculated by the following equation:

$$\gamma_i = \frac{\sum_{n=1}^{N} |y_i^{(n)} y_m^{*(n)}|}{\sqrt{\sum_{n=1}^{N} |y_i^{(n)}|^2 \sum_{n=1}^{N} |y_m^{(n)}|^2}} \tag{8}$$

In the Equation (8), N indicates the number of pixels in an estimation window; $y_i^{(n)}$ and $y_m^{(n)}$ represent the nth complex signal of the estimation window in the ith SAR image and the master SAR image; and, $\hat{\gamma}_i$ is the average coherence of all the pixels. After separating the thermal dilation from the infrastructures, the deformation maps of research targets are available and separately show the thermal dilation and trend deformation.

In this study, the estimated thermal dilations were validated in two ways. Qualitatively, their spatial patterns were compared with the patterns predicted from the specific structural mechanical properties of infrastructures. Quantitatively, the thermal dilation coefficients that were estimated from both the traditional method and our method using Equation (9) were compared with the actual physical properties of materials, which indicates the greater reliability of our method.

$$D_T = \alpha_T L \Delta T \tag{9}$$

where D_T indicates the magnitude of the thermal dilation along its transmission direction; α_T is the thermal dilation coefficient of the material; and, L is the effective transmission length of the thermal dilation.

Moreover, the thermal dilation characteristics, in terms of their transmission direction, spatial pattern, and magnitude were analysed to identify their potential correlation with the specific structural characteristics of different infrastructure types. These analytical findings aid in better understanding the thermal dilation evolution process of different civil infrastructure types and are valuable in optimizing their future maintenance strategies.

3. Case Studies and Preliminary Results

The method described above has been applied to three case studies concerning different infrastructure types, including the Shanghai World Financial Center (SWFC) building, the Shanghai

New International Expo Center (SNIEC) buildings, and the Hong Kong Tsing Kwai Highway (TKH). For each case, we briefly introduced the SAR data and interpreted the thermal dilation result in detail.

3.1. Skyscraper

3.1.1. The SWFC and SAR Data

The SWFC is a skyscraper building with the world's highest viewing platform of approximately 492 m, which ranks as the seventh highest building in the world. The optical picture and the SAR amplitude image of this building are shown in Figure 3a,b, respectively. In this case, a stack of 24 descending TerraSAR-X Stripmap mode images with approximately 3 m resolution was collected from 2014 to 2016 over Shanghai. The coverage of the TerraSAR-X images and the location of the SWFC are illustrated in Figure 3c. Leveling points F59 and F16 near the building (see triangles in Figure 3c) were used to validate the DInSAR results [21]. The basic SAR image information is described in Table 1, and the temperatures were acquired from the China Meteorological Data Sharing Service Website.
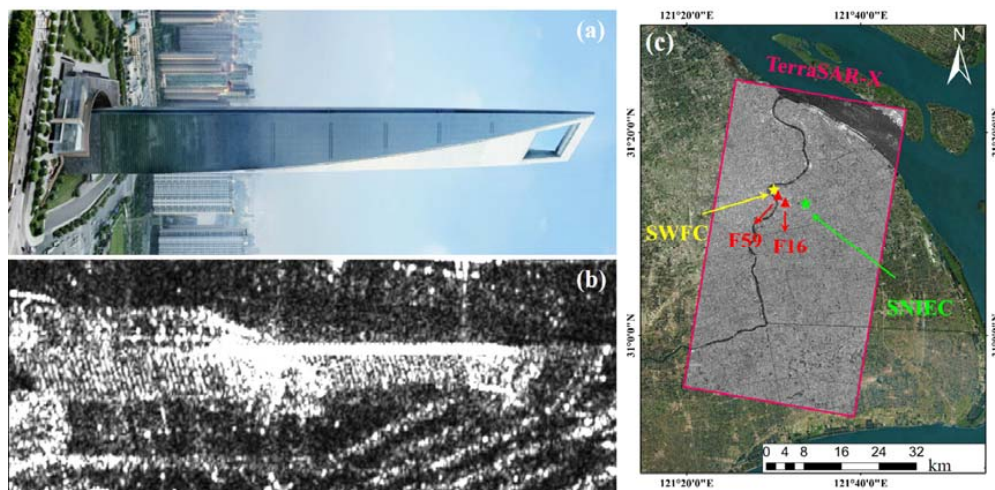

Figure 3. (**a**) The optical picture of the Shanghai World Financial Center (SWFC); (**b**) the SAR amplitude image of the SWFC; and, (**c**) the coverage of TerraSAR-X images in the Google Map (red rectangle), the yellow star indicates the location of the SWFC and the green star represents the SNIEC described in the following, the red triangles are the leveling points.

Table 1. Basic information of TerraSAR-X images in Shanghai.

No	Date	Perpendicular Baseline (m)	Temporal Baseline (Days)	Acquisition Temperature (°C)
1	2 August 2014	−34.3	−385	26.3
2	24 August 2014	−74.1	−363	25.4
3	15 September 2014	−94.9	−341	26.5
4	7 Octorber 2014	−179.7	−319	23.9
5	29 Octorber 2014	−186	−297	12.4
6	1 December 2014	−104.4	−264	4.7
7	23 December 2014	−32.7	−242	8.1
8	10 March 2015	−35.3	−165	6.9
9	1 April 2015	−45.8	−143	12.1
10	15 May 2015	22.9	−99	27.2
11	27 June 2015	52.3	−55	25.3
12	20 July 2015	−126.2	−33	24.1
13	22 August 2015	0	0	21.9
14	24 September 2015	−43.9	33	26.1
15	27 Octorber 2015	255.8	66	20.8

No	Date	Perpendicular Baseline (m)	Temporal Baseline (Days)	Acquisition Temperature (°C)
16	29 November 2015	−87.3	99	9.2
17	21 December 2015	−54.4	121	7.1
18	29 March 2016	−112.4	220	10.6
19	1 May 2016	−94	253	16.3
20	3 June 2016	17.4	286	17.8
21	6 July 2016	−110.8	319	28.6
22	8 August 2016	−33.8	352	26.9
23	10 September 2016	121.2	385	24.2
24	13 Octorber 2016	64.4	418	19.2

3.1.2. Thermal Dilation Results

Based on our method, the estimated topography is close to the real height of 492 m and it is considered to be reliable. The time series differential interferometric phases of the SWFC are obtained and shown in Figure 4. Interferometric fringes with different densities along the building were observed in the differential interferograms with various temperature differences (ΔT). Specifically, when the ΔT is large, several fringes can be observed in the interferograms, which are shown by the red rectangles in Figure 4. This periodical phase changing disappeared or became slower in the differential interferograms with a smaller ΔT, implying that these periodical fringes are mainly affected by the change in temperature. Moreover, the thermal dilation of the SWFC is most likely to propagate in the vertical direction because the fringes evidently transmitted along the vertical direction of the building.
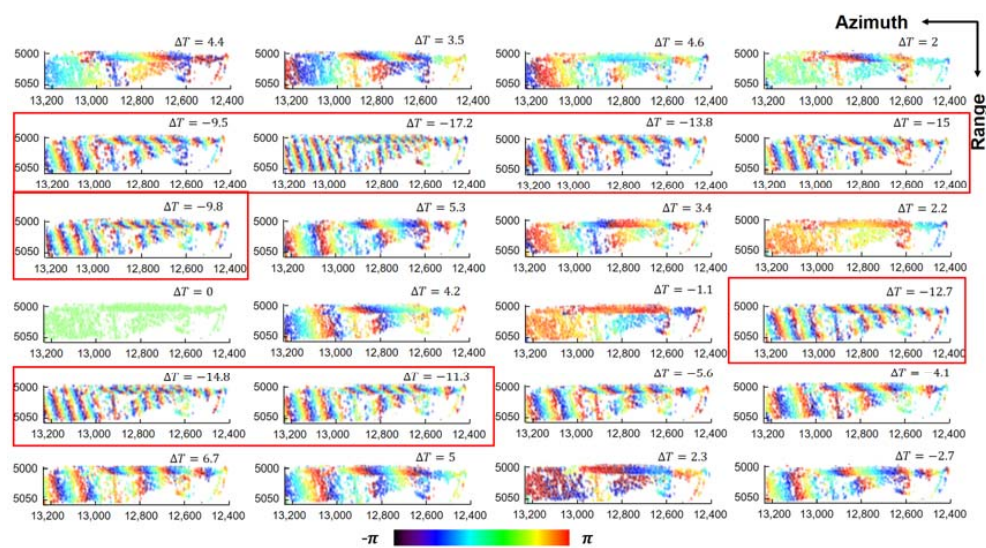

Figure 4. The time series differential interferograms of the SWFC, the red rectangles indicate the differential interferograms with larger temperature differences and denser fringes.

Since the thermal dilation of the SWFC is mainly along the vertical direction, the time series vertical deformations of this building were calculated and are shown in Figure 5. The PTs distribution achieved an excellent coverage of the entire building, thus ensuring a robust estimation of the deformation parameters. From the structural point of view, the bottom of the building is supposed to be a fixed point because the displacement at the bottom of the building is very small and gradually increases to the top. Periodical displacements of the building can be observed during the observation period, especially on the top half of it, with values ranging up to approximately 90 mm. The positive values indicate

that the rising temperature induces an increase in the building's height, leading to the displacement towards the satellite, and vice versa.
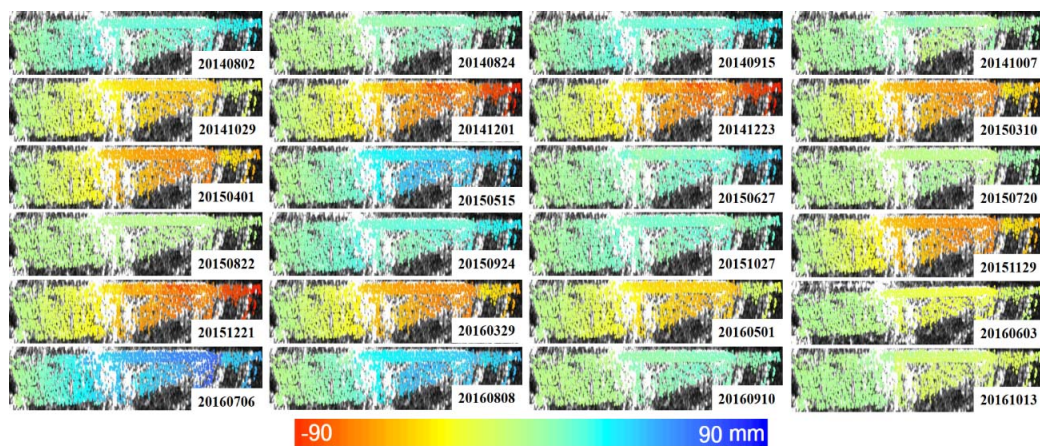

Figure 5. The time series vertical displacements of the SWFC.

We obtained the vertical length variation of the building by calculating the average deformation difference (ΔD) between the bottom and top PTs (blue dots in Figure 6), and found that it is highly correlated with the acquisition temperature (T). The standard deviation of the measurements calculated at each acquisition time is shown as an error bar that is marked by an orange line. Both the traditional least squares estimation and the robust coherence-weighted least squares regression analysis proposed in this study were implemented to identify the relationship between these two variables. The two linear fitting models established by the traditional method (green dotted line) and our method (red solid line), which are shown in Figure 6, clearly highlighted the evident linear correlation between the ΔD and T.
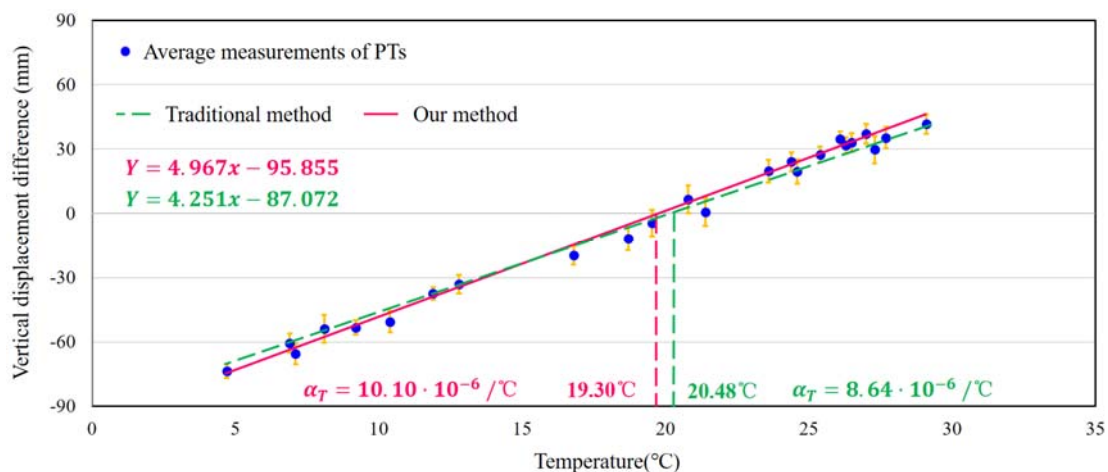

Figure 6. The thermal dilation model of the SWFC.

According to these two models, when ΔD equals to zero, the corresponding T is 20.48 °C for the traditional method and 19.30 °C for our method, which are both close to the temperature of the master image (21.9 °C). Although the fitted reference temperature (without thermal dilation) of the traditional method is closer to 21.9 °C than our method, the accuracy of only one measurement was considered. However, deformation measurements that are close to the reference temperature would be less accurate than those with larger temperature differences. Actually, when the temperature is approximately 21.9 °C (like ±3 °C), the temperature of the building does not change that much. Thus,

the corresponding thermal dilation will be small, and the accuracy would be low. When the temperature differences are larger than 10 °C, the building will undergo significant temperature changes, and the thermal dilation is evident and not susceptible to noise. Therefore, we use the linear thermal dilation coefficients of the construction material calculated from the fitted models (8.64×10^{-6} per °C for the traditional method and 10.10×10^{-6} per °C for our method), which consider the total accuracy of all measurements, to evaluate the results. Since the actual thermal dilation coefficient is taken as 12×10^{-6} per °C for pure steel and 9×10^{-6} per °C for pure concrete [40], the coefficient derived from our method (10.10×10^{-6} per °C) is within the reasonable range of the physical properties of typical steel and reinforced concrete material ($9 \sim 12 \times 10^{-6}$ per °C), while the coefficient derived from the traditional method is lower than the theoretical value. According to the thermal dilation coefficient validation, our method is proven to be more effective than the traditional method.

After calibrating and validating based on the local leveling points, the trend deformation and thermal dilation of the SWFC are obtained and are shown in Figure 7a,b, respectively. After separating the thermal dilation, this building is quite stable with a slight and uniform subsidence velocity of less than 5 mm/year, which indicates that the observed time series displacement is mainly caused by thermal dilation. The temperature deformation parameters are around zero at the bottom of the building and gradually increased from the bottom to approximately 5 mm/°C at the top.
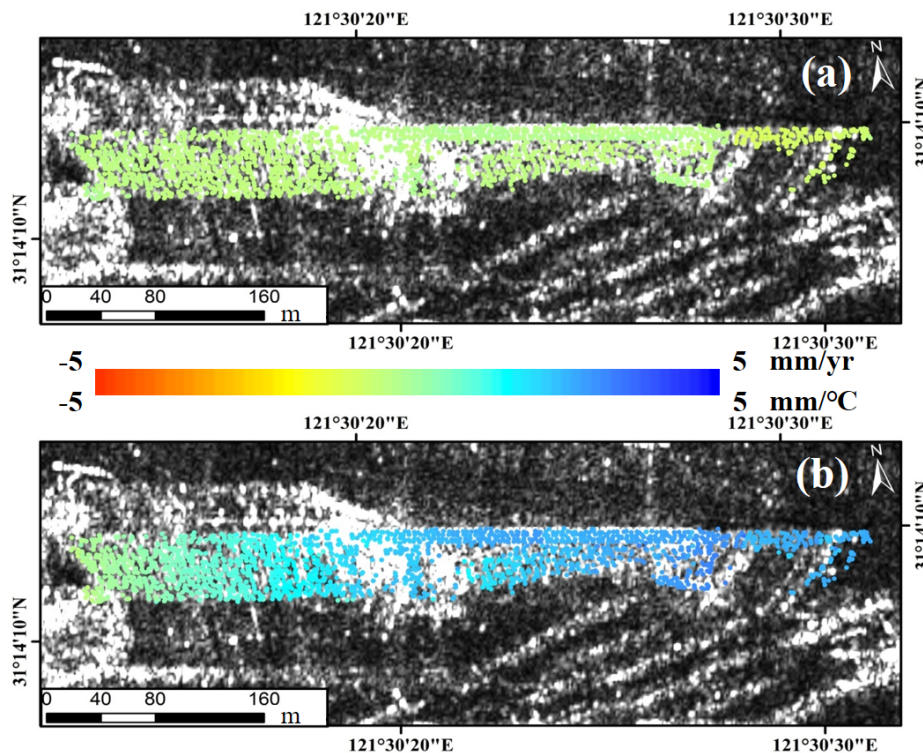

Figure 7. The (**a**) trend deformation and (**b**) thermal dilation of the SWFC.

3.2. Low Buildings

3.2.1. The SNIEC and SAR Data

The SNIEC is the international exhibition venue in the heart of Shanghai, which consists of 17 exhibition halls, including W1 to W5 in the west, N1 to N5 in the north, and E1 to E7 in the east (see Figure 8b). Each exhibition hall is approximately 185 m long and 70 m wide, with an entire indoor area of 200,000 square meters and an outdoor area of 130,000 square meters. The amplitude image and the optical image of these buildings are shown in Figure 8a,b, respectively. Each exhibition hall is clearly visible in the high-resolution SAR image. The same SAR dataset (see Figure 3c) with the

SWFC was used for the thermal dilation monitoring, and the location of the SNIEC is represented as the green star in Figure 3c.
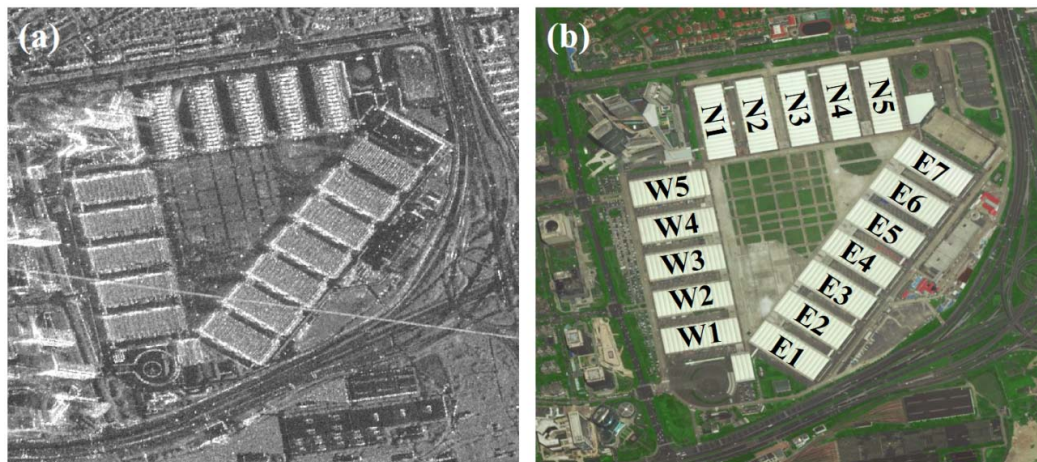

Figure 8. The (**a**) amplitude and (**b**) Google-Earth optical image of the Shanghai New International Expo Center (SNIEC).

3.2.2. Thermal Dilation Results

The time series differential interferograms of SNIEC are illustrated in Figure 9, where the denser periodical fringes appeared at the top of exhibition halls in the differential interferograms with larger temperature differences (remarked by red rectangles). Since there are no obvious elevation differences between the two sides of the exhibition halls, and the distance between the two sides is less than 200 m, these fringes cannot be caused by the topographic phase or the atmosphere phase. According to the temperature correlation analysis of each differential interferogram, the thermal dilation is probably the main cause of these fringes. If the thermal dilation of the exhibition halls was mainly transmitted along the vertical direction, the thermal dilation magnitude at the top of buildings with almost the same height should be the same. However, the magnitudes of the thermal dilation at the top of the exhibition halls are different from one side to the other side in the differential interferograms, which indicates that the thermal dilation is most likely to propagate along the horizontal direction.

Based on the above analysis, we assumed that the thermal dilation of the exhibition halls was mainly transmitted in the horizontal direction. The time series east-west displacements of the SNIEC were then calculated and they are shown in Figure 10. First, we can see that the number of detectable PTs depends on their projection lengths in the north-south direction, which is related to the satellite's flying direction (nearly north-south). The most PTs were selected from the exhibition halls N1 to N5 since they were nearly along the north-south direction, while fewer PTs were identified at the tops of W1 to W5 and E1 to E7 due to their shorter projection lengths along the flying direction of the satellite, especially for the five exhibition halls in the west.

According to Figure 10, the deformation in the middle of the building is small and gradually increased to both sides, with values ranging up to approximately 20 mm, but in opposing directions. Since the transmission distances of the thermal dilation in the east-west direction are different for different exhibition halls, their thermal dilation magnitudes are also slightly varied. The thermal dilation of the north exhibition halls (N1 to N5) is smaller when compared with the west (W1 to W5) and east (E1 to E7) halls, due to the smaller scales along the east-west direction. When we further converted the east-west deformation to the length direction of each exhibition hall, a linear relationship between the average displacements in the length direction of exhibition halls (see blue dots in Figure 11) and the corresponding temperature variation was found.
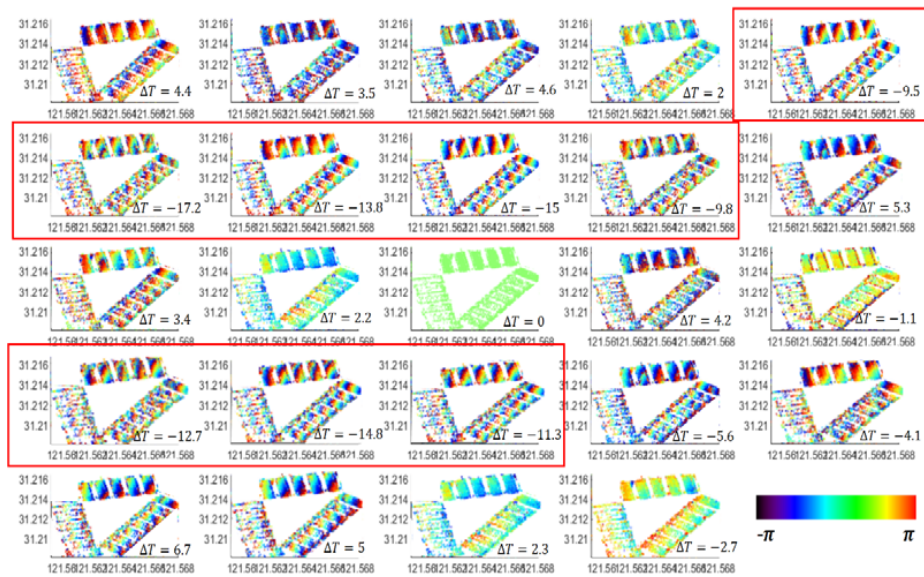
Figure 9. The time series differential interferograms of the SNIEC, the red rectangles indicate the differential interferograms with larger temperature differences and denser fringes.
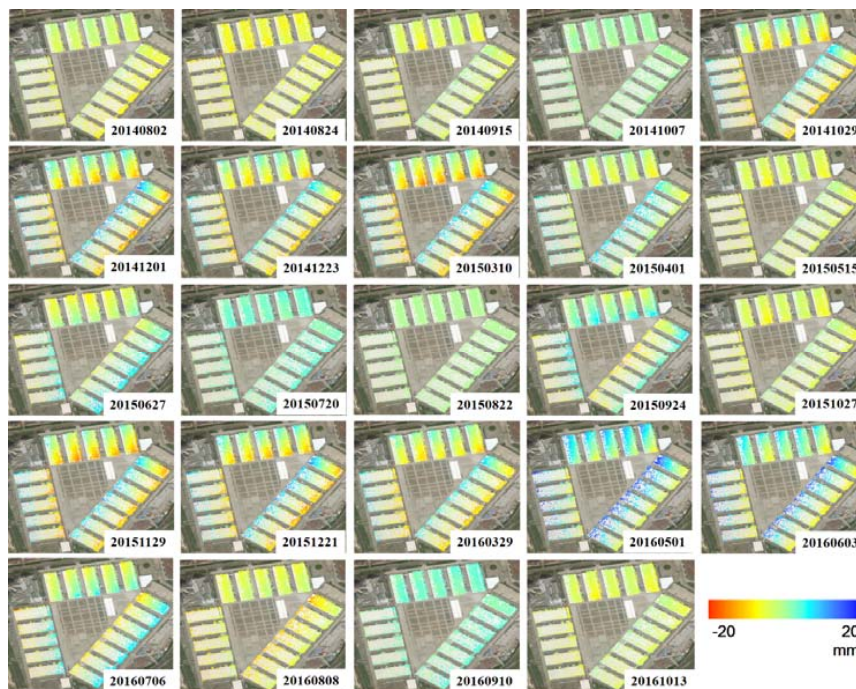

Figure 10. The time series horizontal displacements of the SNIEC.

The estimated thermal dilation models of the SNIEC are shown in Figure 11, where the green dotted line indicates the model derived from the traditional method and the red solid line indicates the model that was calculated using our method. The error bars, which represented by orange lines, indicate the standard deviation of measurements at each acquisition. According to these models, when the air temperature is approximately 21.52 °C in the traditional model or 21.32 °C in our model, there is no thermal dilation detected. Both of the models are close to the measured value of 21.9 °C. Based on this temperature, when the temperature changed by 1 °C, the thermal dilation of 8.77×10^{-6} (traditional model) and 9.80×10^{-6} (our model) of the building's length will be detected.

The coefficient estimated from our method (9.80×10^{-6} per °C) is also in accordance with the linear thermal dilation coefficient of steel and reinforced concrete material, while that of the traditional method (8.77×10^{-6} per °C) is still slightly smaller than the theoretical value, which implies the greater reliability of our method.
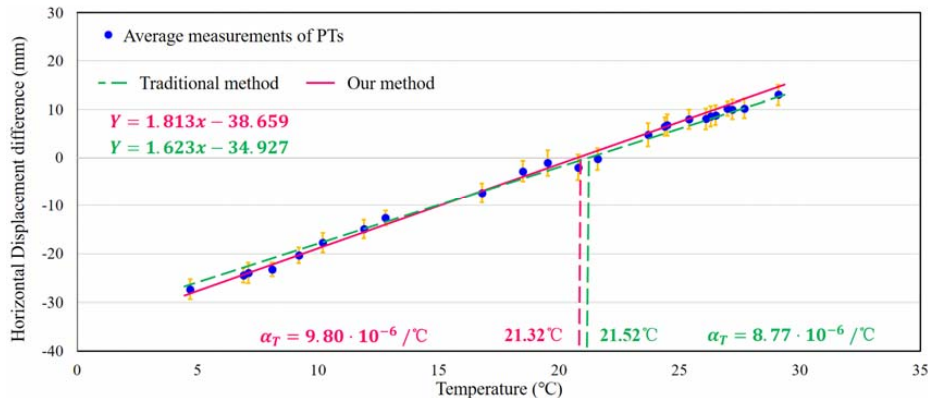

Figure 11. The thermal dilation model of the SNIEC.

After calibrating and validating based on the local leveling points, the trend deformation and thermal dilation of the SNIEC buildings are illustrated in Figure 12a,b, respectively. The magnitude of the temperature deformation parameters on the exhibition halls increased from the middle of the buildings to approximately 1 mm/°C at both sides, but with opposing directions. From such a thermal dilation spatial pattern, we can infer that, structurally, the fixed points of the buildings are probably located in the middle of the roofs, and the thermal dilation transmitted from the middle to both sides reached the peak at both ends. The trend deformations of these buildings are small, ranging from −4 to 4 mm/year, which may be caused by the surface subsidence of Shanghai. Therefore, the thermal dilation is the main cause of the observed time series deformation. The slightly different trend deformation of the exhibition halls may be due to their different orientations.
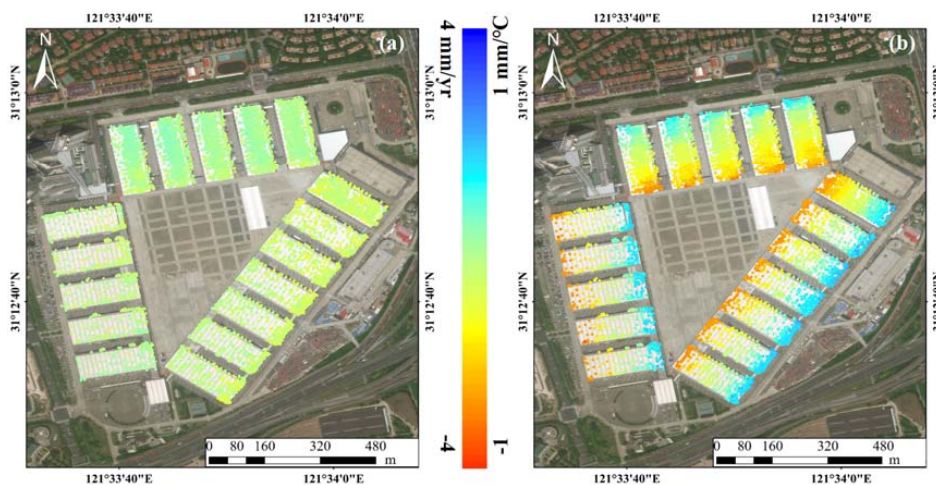

Figure 12. The (**a**) trend deformation and (**b**) thermal dilation of the SNIEC.

3.3. Highway

3.3.1. The TKH and SAR Data

The TKH in Hong Kong is an elevated road, which is approximately 20 m above the ground. The optical image and SAR amplitude image of TKH are shown in Figure 13a,b, respectively. The blue

rectangles in Figure 13a indicate the locations of the expansion joints of the TKH. In this study, we collected 28 TerraSAR-X Stripmap images from 2013 to 2014 in order to monitor the highway's thermal dilation. The coverage of the SAR images and the location of the highway are illustrated in Figure 13c. The basic information of the SAR images is described in Table 2.
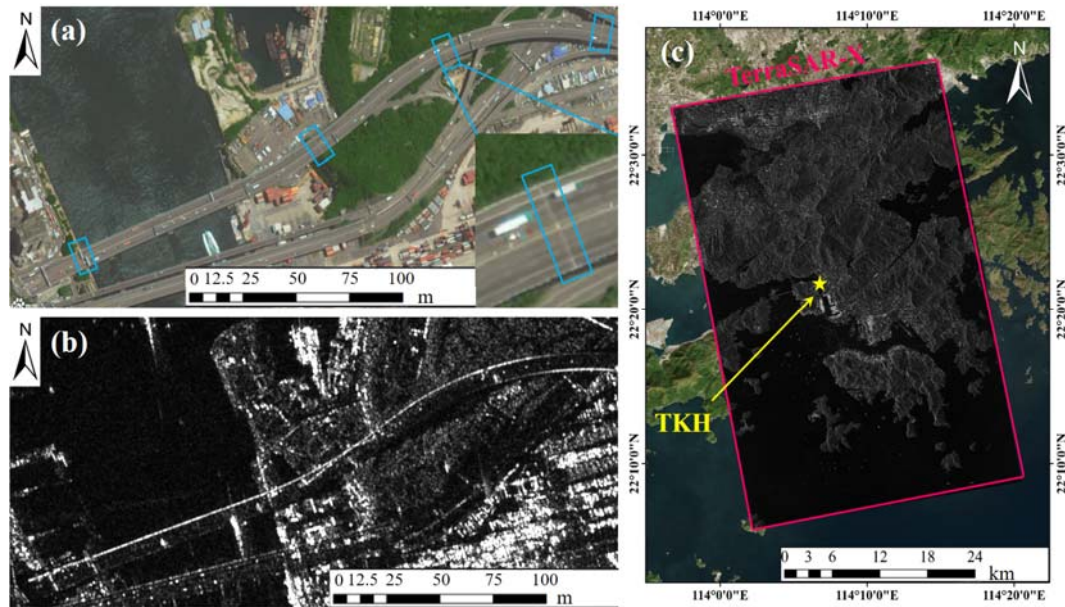

Figure 13. (**a**) The optical image of the Tsing Kwai Highway (TKH), the blue rectangles represent the locations of expansion joints; (**b**) the SAR amplitude image of the TKH; and, (**c**) the coverage of TerraSAR-X images in the Google Map (red rectangle), the yellow star indicates the location of the TKH.

Table 2. Basic information of TerraSAR-X images in Hong Kong.

No	Date	Perpendicular Baseline (m)	Temporal Baseline (Days)	Acquisition Temperature (°C)
1	7 July 2013	63	−143	29.4
2	18 July 2013	−40.3	−132	29.8
3	29 July 2013	227.6	−121	31.1
4	9 August 2013	141.6	−110	30.9
5	20 August 2013	159.1	−99	29.3
6	31 August 2013	158	−88	27.7
7	22 September 2013	126.5	−66	27.0
8	3 Octorber 2013	184.5	−55	24.1
9	14 Octorber 2013	150	−44	23.8
10	25 Octorber 2013	103.7	−33	20.5
11	5 November 2013	160.1	−22	22.7
12	16 November 2013	132.4	−11	19.8
13	27 November 2013	0	0	16.2
14	8 December 2013	−41.6	11	17.8
15	19 December 2013	141.6	22	11.5
16	30 December 2013	39.9	33	8.4
17	21 January 2014	30.2	55	12.3
18	1 February 2014	−13.9	66	22.0
19	12 February 2014	178.4	77	8.5
20	23 February 2014	221.9	88	13.4
21	28 March 2014	240.3	121	23.7
22	30 April 2014	−36.4	154	26.6
23	11 May 2014	156.9	165	29.8
24	13 June 2014	69.4	198	29.3
25	24 June 2014	78	209	30.5

3.3.2. Thermal Dilation Results

The time series differential interferometric phases of the TKH are shown in Figure 14. Although the annual temperature difference in Hong Kong is smaller than that of Shanghai, the temperature-dependent deformation can also be detected by the X-Band SAR images. The differential interferograms with temperature differences that are larger than 10 °C showed denser fringes than others, and those fringes changed more slowly in the differential interferograms with smaller temperature differences. Therefore, these fringes are most likely caused by the thermal dilation. According to their spatial pattern, the thermal dilation is probably transmitted along the longitudinal direction of the TKH.

The longitudinal time series displacement maps of the TKH are shown in Figure 15. Dense PTs were selected on the TKH, especially on the northern outline, which is very bright in the SAR amplitude image. In this case, several sudden discontinuities along the highway were observed and are marked by the red lines in Figure 15. Based on further analysis, these discontinuities appear to be located at the expansion joints of the TKH, which are represented in Figure 13a. By referring to the red lines, this highway can be divided into three segments, which correspond to the Cheung Tsing Bridge and two segments of viaducts from the west to the east. The accumulation of thermal dilation in the two terminations of the Cheung Tsing Bridge is evident. The thermal dilations of the two highway segments transmitted from one expansion joint to another. From a structural viewpoint, this structure is defined in the civil engineering framework as a hyperstatic structure, meaning that the high number of constraints (such as expansion joints) tend to hinder the deformation of the bridge and highway [18,28,29]. Therefore, such a spatial pattern of thermal dilation agreed well with the pattern predicted from the positions of expansion joints along the highway, which indicates the reliability of our results.
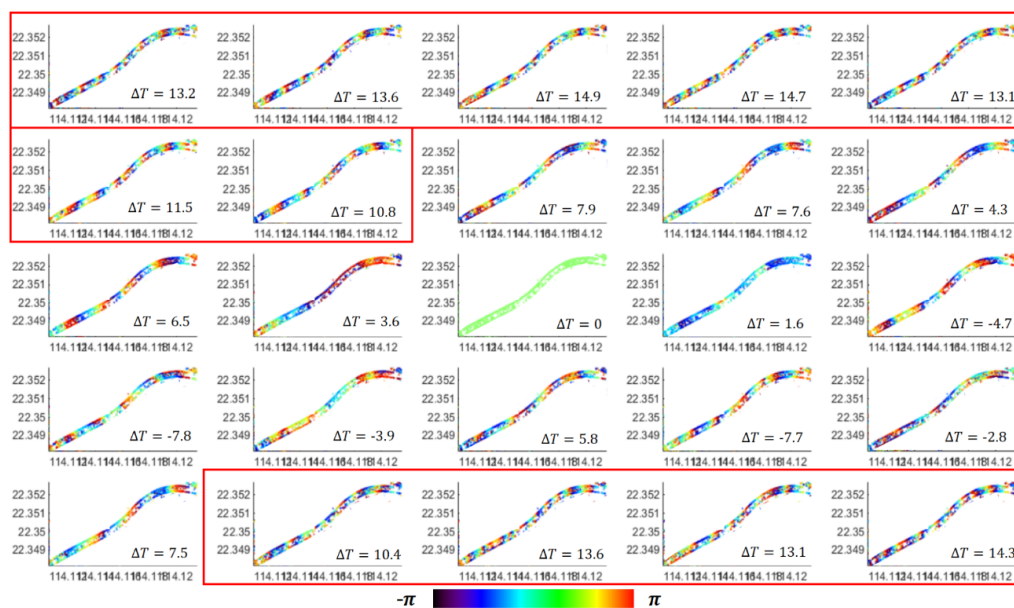

Figure 14. The time series differential interferograms of the TKH, the red rectangles indicate the differential interferorgrams with larger temperature differences and denser fringes.

By quantitatively analysing the time series average longitudinal displacements of the Cheung Tsing Bridge (blue dots in Figure 16) and the temperature variation, the thermal dilation model that was derived from the traditional least squares method and our coherence-weighted method for the TKH are illustrated in Figure 16 as the green dotted line and red solid line, respectively. According to these models, when the air temperature is approximately 17.24 °C for the traditional model and 16.92 °C for our model, no thermal dilation is observed on the highway. Both the traditional method and our

method comprehensively consider all of the measurements at different temperatures to minimize the total errors, rather than only considering the measurement with no thermal dilation. Therefore, the measurements are not always exactly the same as the fitted values, and the slight differences in the no thermal dilation temperature are within a reasonable range. Based on the standard temperature, a temperature variation of 1 °C may lead to a change of 8.15×10^{-6} and 9.37×10^{-6} of the bridge's length, according to the traditional model and our model. The linear thermal dilation coefficient estimated from our method (9.37×10^{-6} per °C) is within the reasonable range of the construction material physical properties, while that of the traditional model (8.15×10^{-6} per °C) is again slightly smaller than the theoretical model, which indicates the reliability of our method.
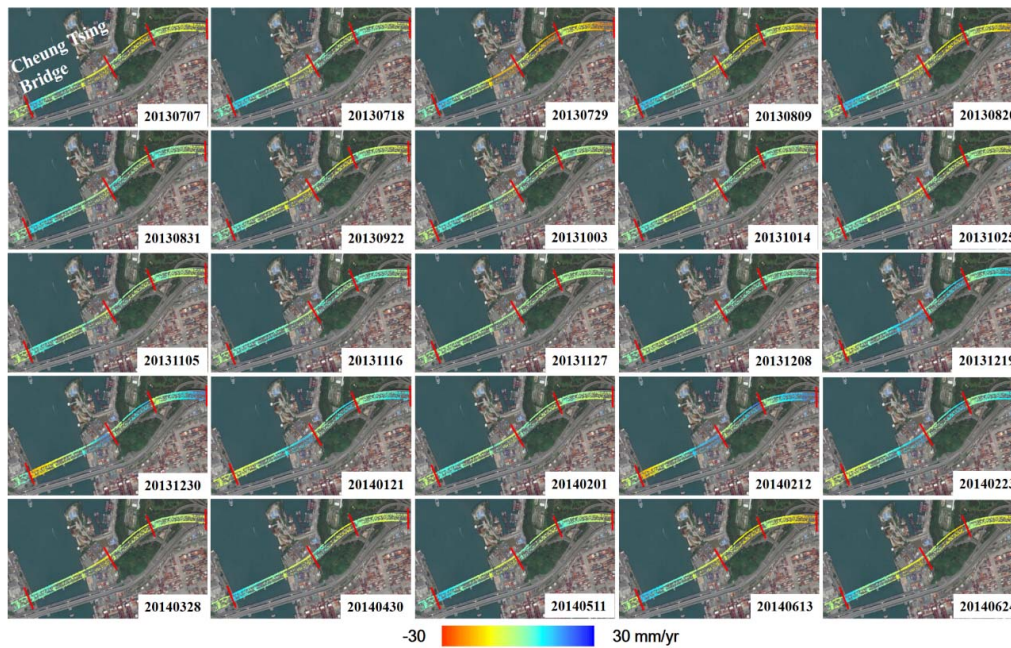

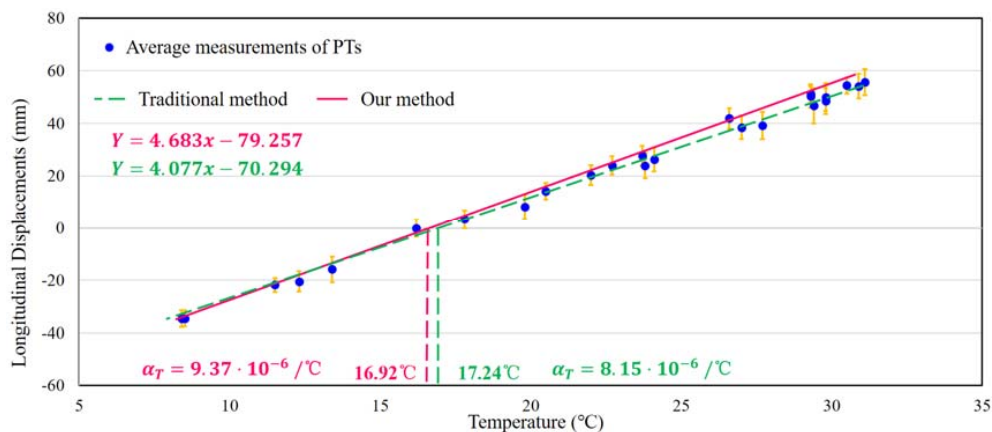**Figure 15.** The time series longitudinal displacements of the TKH.

Figure 16. The thermal dilation model of the TKH.

After modelling and separating the thermal dilation using our method, the trend deformation and thermal dilation of the TKH are calculated and are shown in Figure 17a,b, respectively. Clearly, the TKH is quite stable during the observation period, especially on the highway segment, and a slight trend deformation of less than 5 mm/year was observed on the Cheung Tsing Bridge. The temperature deformation parameters varied from −2.5 to 2.5 mm/°C and propagated longitudinally on each sub-segment. The thermal dilation of the Cheung Tsing Bridge gradually increased from the middle to

both ends with opposing directions. The thermal dilation stopped at the locations of the expansion joints and started to transmit again in the next segment because the expansion joints in the TKH hindered the thermal dilation transmission.
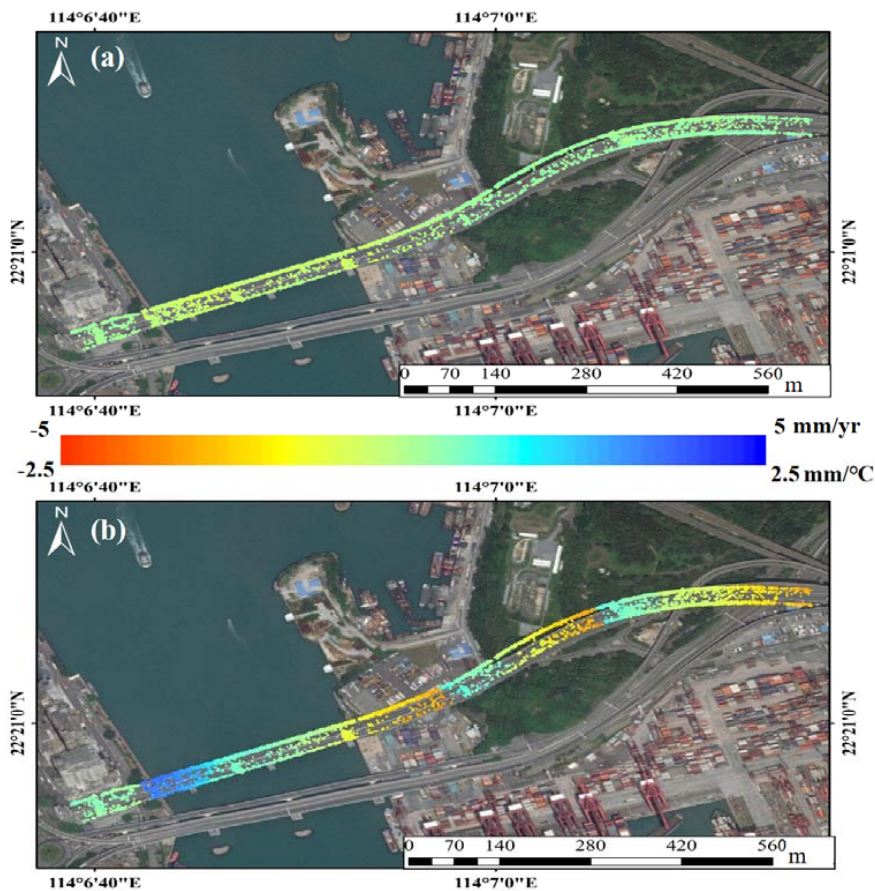

Figure 17. The (**a**) trend deformation and (**b**) thermal dilation of the TKH.

4. Discussion of Thermal Dilation Mechanisms

To further investigate the thermal dilation evolution process, an in-depth analysis was developed by summarizing the thermal dilation results of different civil infrastructures types. Then, the common characteristics of civil infrastructure thermal dilations were concluded and are illustrated in Table 3, which provides valuable information for the engineers to conduct thermal dilation related research in the future.

Table 3. The thermal dilation mechanisms for civil infrastructures.

Thermal Dilation Mechanisms	The SWFC	The SNIEC	The TKH	Common
Transmission direction	Vertical	Horizontal	Horizontal	Longest side direction in geometry shape
Spatial pattern	Increased gradually from the bottom of building	Increased gradually from the middle of buildings but with opposite directions	Increased gradually from the middle of bridge but discontinuity at expansion joints	Provide the locations of structural key points
Magnitude	Largest	Smallest	Middle	Associated with materials and sizes

First, according to the three case studies, we found that the transmission direction of thermal dilation is highly dependent on the specific structural shape of the target, and it tends to transmit along

the direction of the longest side of the structures' geometric shape. Since the shape of the SWFC is very long in the vertical direction but is much shorter in the horizontal direction, the thermal dilation fringes mainly changed in the building's vertical direction. However, as far as the SNIEC and TKH are concerned, they are longer in the horizontal direction, but are much shorter in the vertical direction. Therefore, their thermal dilations are mainly accumulated along the horizontal direction, especially in the longitudinal directions. In general, the thermal dilations of vertical infrastructures, such as skyscrapers, tend to transmit along the vertical direction, while those of the horizontal infrastructures, such as low buildings and highways, are proven to propagate in the horizontal direction.

Second, the spatial pattern of thermal dilation can provide valuable information regarding the static structural characteristics of infrastructures, such as the positions of structural key points. As for the SWFC, the temperature deformation parameter approximately equals zero at the bottom and increased gradually to the maximum value at the top, indicating that the bottom on the ground is probably the fixed point of the building and the top of the building is structurally free. In terms of the SNIEC, the temperature deformation parameter remains zero in the middle of the exhibition halls and it increased gradually to both sides with opposing values, which indicates that the fixed points are most likely located in the middle of the buildings, while both sides are structurally free. Regarding the TKH, the discontinuities of the temperature deformation parameter indicated the locations of the expansion joints along the highway, because these constraints hindered the accumulation of thermal dilation [18,27,28]. Therefore, the locations of structural key points along infrastructures can be approximately inferred from the estimated thermal dilation patterns.

Finally, the magnitude of thermal dilation is associated with the materials and sizes of infrastructures. Since the thermal dilation showed a highly linear correction with the temperature variation, it can be modelled while using a linear regression model. Based on the analysis of the thermal dilation model, two types of information would affect the thermal dilation magnitude. On the one hand, the thermal dilation coefficients of different material specifications are slightly different, which would affect the magnitude of the accumulated thermal dilation within a certain temperature range. On the other hand, the size of the structures also affects the magnitude of the accumulated thermal dilation. The thermal dilation can increase to a large value when there are no extra constraints on the structures, while it would be limited to a smaller value when extra constraints shorten the transmission size. Therefore, with the same temperature difference and similar building material, such as the SWFC and SNIEC, the accumulated thermal dilation of the SWFC is larger than that of SNIEC because the longer effective thermal dilation transmission distance would lead to a larger accumulation of thermal dilation in the structures.

5. Conclusions

Given the advantages of richer ground target information and a higher sensitivity to the small deformations in the high-resolution SAR images, a multi-temporal DInSAR approach, which estimates the civil infrastructure thermal dilations with an increasing number of PTs and high-resolution topography estimation based on TerraSAR-X images, was applied in this study. Both the coherent and incoherent information derived from the high-resolution SAR images, and the semantic information of the specific structures were integrated into the DInSAR method in order to refine the PTs identification. Moreover, the interferometric subsets with small temporal baselines and temperature differences were used for the high-resolution topography estimation of modern civil infrastructures. Then, a two-step analysis method consisting of a model analysis phase and a model generation phase was applied to estimate the thermal dilation. First, a pre-analysis was adopted to determine the transmission direction, spatial pattern, and temporal variation of thermal dilation. Then, both the traditional least squares regression analysis and the robust coherence-weighted least squares regression analysis proposed in this study were performed to quantitatively estimate the thermal dilation model. In all cases studies, the thermal dilation models that were estimated from the two methods were validated in terms of the estimated linear thermal dilation coefficients, which indicate the greater reliability of our method.

Furthermore, the general thermal dilation characteristics of different civil infrastructure types were explored by analysing the potential relationship between the thermal dilation results and their specific structural characteristics. Our results demonstrate that the thermal dilation transmission direction is highly dependent on the specific structural shape of the target, and it tends to transmit along the longest side direction of the structures' geometric shape. Moreover, the static structural characteristics of infrastructures, such as the locations of structural key points, can be approximately inferred from the thermal dilation spatial patterns. Finally, the thermal dilation magnitude is associated with the materials and the sizes of the objects. The thermal dilation characteristics of different civil infrastructure types that are explored in this study can provide valuable information for better understanding the thermal dilation evolution process, and these findings are instructive for the future related work.

Author Contributions: All five authors contributed to this work. X.Q. processed the datasets, implemented the methodology, and finished the manuscript. L.Z. guided the results discussion and interpretation. X.D. and M.L. supervised the research and provided valuable suggestions for the revision. M.Y. collected and preprocessed the SAR images and acquisition temperatures.

Conflicts of Interest: The authors declare no conflict of interest.

References

1. Cusson, D.; Ghuman, P.; Mccardle, A. Satellite sensing technology to minitor bridges and other civil infrastrucures. In Proceedings of the 5th International Conference on Strucural Hwalth Monitoring of Intelligent and other Civil Infrastructres (SHMII-5), Cancun, Mexico, 4–8 December 2011; pp. 1–9.
2. Chang, L.; Hanssen, R.F. Detection of cavity migration and sinkhole risk using radar interferometric time series. *Remote Sens. Environ.* **2014**, *147*, 56–64. [CrossRef]
3. Lan, H.; Li, P.; Liu, H.; Yang, Z. Complex urban infrastructures deformation monitoring using high resolution PSI. *IEEE J. Sel. Top. Appl. Earth Obs. Remote Sens.* **2012**, *5*, 643–651. [CrossRef]
4. Arangio, S.; Calo, F.; Mauro, M.D.; Bonano, M.; Marsella, M.; Manunta, M. An application of the SBAS-DInSAR technique for the assessment of structural damage in the city of Rome. *Struct. Infrast. Eng.* **2014**, *10*, 1469–1483. [CrossRef]
5. Wang, H.; Chang, L.; Markine, V. Structural health monitoring of railway transition zones using satellite radat data. *Sensors* **2018**, *18*, 413. [CrossRef] [PubMed]
6. Beshr, E.; Kallop, M. Monitoring bridge deformation using auto-correlation adjustment technique for total station observations. *Positioning* **2013**, *4*, 1–7. [CrossRef]
7. Ferretti, A.; Prati, C.; Rocca, F. Permanent scatterers in sar interferometry. *IEEE Trans. Geosci. Remote Sens.* **2001**, *39*, 8–20. [CrossRef]
8. Berardino, P.; Fornaro, G.; Lanari, R.; Sansosti, E. A new algorithm for surface deformation monitoring based on small baseline differential sar interferograms. *IEEE Trans. Geosci. Remote Sens.* **2002**, *40*, 2375–2383. [CrossRef]
9. Jiang, Y.; Liao, M.; Wang, H.; Zhang, L.; Balz, T. Deformation monitoring and analysis of the geological enrionment of Pudong International Airport with persistent scatterer SAR interferometry. *Remote Sens.* **2016**, *8*, 1021. [CrossRef]
10. Bai, L.; Jiang, L.; Wang, H.; Sun, Q. Spatiotemporal characterization of land subsidence and uplift (2009–2010) over Wuhan in central China revealed by TerraSAR-X InSAR Analysis. *Remote Sens.* **2016**, *8*, 350. [CrossRef]
11. Hooper, A. A statistical-cost approach to unwrapping the phase of InSAR time series. In Proceedings of the Inernational Workshop on ERS SAR Interferometry, Frascati, Italy, 30 November–4 December 2009.
12. Hooper, A. A multi-temporal InSAR method incorporating both scatterer and small baseline approaches. *Geophys. Res. Lett.* **2008**, *35*, L16302. [CrossRef]
13. Hooper, A. Persistent Ascatter Radar Interferometry for Crustal Deformation Studies and Modelling of Volcanic Deformation. Ph.D. Thesis, Stanford University, Stanford, CA, USA, 2006.

14. Milillo, P.; Giardina, G.; Matthew, J.; Perissin, D.; Milillo, G. Multi-temporal InSAR structural damage assessment: The London crossrail case study. *Remote Sens.* **2018**, *10*, 287. [CrossRef]

15. Ma, P.; Lin, H. Robust detection of single and double persistent scatterers in urban built environments. *IEEE Trans. Geosci. Remote Sens.* **2016**, *54*, 2124–2139. [CrossRef]

16. Eineder, M.; Adam, N.; Bamler, R.; Yague, M.; Breit, H. Spaceborne spotlight SAR interferometry with TerraSAR-X. *IEEE Trans. Geosci. Remote Sens.* **2009**, *47*, 1524–1535. [CrossRef]

17. Gernhardt, S.; Adam, N.; Eineder, M.; Bamler, R. Potential of very high resolution SAR for persistent scatterer interferometry in urban areas. *Geogr. Inf. Sci.* **2010**, *16*, 103–111. [CrossRef]

18. Daniele, P.; Wang, Z.; Lin, H. Shanghai subway tunnels and highways monitoring through Cosmo-SkyMed persistent scatterers. *ISPRS J. Photogramm. Remote Sens.* **2012**, *73*, 58–67. [CrossRef]

19. Fornaro, G.; Reale, D.; Verde, S. Bridge thermal dialtion monitoring with millimeter sensitivity via multidimensional SAR imaging. *IEEE Geosci. Remote Sens. Lett.* **2013**, *10*, 677–681. [CrossRef]

20. Shi, X.; Liao, M.; Wang, T.; Zhang, L. Expressway deformation mapping using high-resolution TerraSAR-X images. *Remote Sen. Lett.* **2014**, *5*, 194–203. [CrossRef]

21. Qin, X.; Yang, T.; Zhang, L.; Yang, M.; Liao, M. Health disgnosis of major transporation infrastructures in Shanghai metropolis using high-resolution persistent scatterer interferometry. *Sensors* **2017**, *17*, 2770. [CrossRef] [PubMed]

22. Chang, L.; Dollevoet, R.; Hanssen, R.F. Nationalwide railway monitoring using satellite SAR interferometry. *IEEE J. Sel. Top. Appl. Earth Obs. Remote Sens.* **2017**, *10*, 596–604. [CrossRef]

23. Ma, P.; Lin, H.; Lan, H.; Chen, F. Multi-dimensional SAR tomograpgy for monitoring the deformation of newly built concrete buildings. *ISPRS J. Photogramm. Remote Sens.* **2015**, *106*, 118–128. [CrossRef]

24. Bamler, R.; Eineder, M. The Pyramids of Gizeh seen by TerraSAR-X—A prime example for unexpected scattering mechanisms in SAR. *IEEE Geosci. Remote Sens. Lett.* **2008**, *5*, 468–470. [CrossRef]

25. Gernhardt, S.; Bamler, R. Deformation monitoring of single buildings using meter-resolution SAR data in PSI. *ISPRS J. Photogramm. Remote Sens.* **2012**, *73*, 68–79. [CrossRef]

26. Zhu, J.; Meng, Q. Effeicive and fine analysis for temperature effect of bridges in natural environmentals. *J. Bridge Eng.* **2017**, *22*, 04017017. [CrossRef]

27. Xia, Y.; Chen, B.; Zhou, X.; Xu, Y. Field monitoring and numerical analysis of Tsing Ma suspension bridge termprature behavior. *Struct. Control Health Monitor.* **2013**, *20*, 560–575. [CrossRef]

28. Crosetto, M.; Monserrat, O.; Cuevas-Gonzalez, M.; Devanthery, N.; Luzi, G.; Crippa, B. Measuring thermal expansion using X-band persistent scatterer interferometry. *ISPRS J. Photogramm. Remote Sens.* **2015**, *100* (Suppl. S1), 84–91. [CrossRef]

29. Cuevas, M.; Monserrat, O.; Crosetto, M.; Crippa, B. A new product from persistent scatterer interferometry: The thermal dilation maps. *Urban Remote Sens. Event* **2011**, *50*, 285–288. [CrossRef]

30. Lazecky, M.; Hlavacova, I.; Bakon, M.; Sousa, J.; Perissin, D.; Patricio, G. Bridge displacements monitoring using space-boren X-band SAR interferometry. *IEEE J. Sel. Top. Appl. Earth Obs. Remote Sens.* **2017**, *10*, 205–210. [CrossRef]

31. Qin, X.; Liao, M.; Zhang, L.; Yang, M. Structural health and stability assessment of high-speed railways via thermal dilation mapping with time-series InSAR analysis. *IEEE J. Sel. Top. Appl. Earth Obs. Remote Sens.* **2017**, *10*, 2999–3010. [CrossRef]

32. Reale, D.; Fornaro, G.; Pauciullo, A. Extension of 4-D SAR imaging to thr monitoring of thermally dilation scatterers. *IEEE Trans. Geosci. Remote Sens.* **2013**, *51*, 5296–5306. [CrossRef]

33. Monserrat, O.; Crosetto, M.; Cuevas, M.; Crippa, B. The thermal expansion component of persistent scatterer interferometry observations. *IEEE Gecosci. Remote Sens. Lett.* **2011**, *8*, 864–868. [CrossRef]

34. Goel, K.; Gonzalez, F.R.; Adam, N.; Duro, J.; Gaset, M. Thermal dialtion monitoring of complex urban infrastructure using high resolution SAR data. In Proceedings of the 2014 IEEE International Geoscience and Remote Sensing Symposium (IGARSS), Quebec City, QC, Canada, 13–18 July 2014; pp. 954–957.

35. Zhao, J.; Wu, J.; Ding, X. Elevation extraction and deformation monitoring by multitemporal InSAR of Lupu Bridge in Shanghai. *Remote Sens.* **2017**, *9*, 897. [CrossRef]

36. Wu, J.C.; Hu, F.M. Monitoring ground subsidence along the Shanghai Maglev zone using TerraSAR-X images. *IEEE Geosci. Remote Sens. Lett.* **2017**, *14*, 117–121. [CrossRef]

37. Huang, Q.; Crosetto, M.; Monserrat, O.; Crippa, B. Displacement monitoring and modelling of a high-speed railway bridge using C-band Sentinel-1 data. *ISPRS J. Photogramm. Remote Sens.* **2017**, *128*, 204–211. [CrossRef]

38. Kromanis, R.; Kripakaran, P. Predicting thermal response of bridges using regression models derived from measurement histories. *Comput. Struct.* **2014**, *136*, 64–77. [CrossRef]

39. Huber, P. Robust regression: Asymptotics, conjectures and monte carlo. *Ann. Stat.* **1973**, *1*, 799–821. [CrossRef]

40. Ni, Y.; Hua, X.; Wong, K.; Ko, J.; Asce, F. Assessment of bridge expansion joints using long-term displacement and temperature measuremnt. *J. Perform. Constr. Facil.* **2007**, *21*, 143–151. [CrossRef]